ELECTROCHEMISTRY

Amphiphilic Ti porous transport layer for highly effective PEM unitized regenerative fuel cells

Ahyoun Lim[1,2]**, Hui-Yun Jeong**[1]**, Youngjoon Lim**[1]**, Jin Young Kim**[1,3,4]**, Hee Young Park**[1]**, Jong Hyun Jang**[1,3]**, Yung-Eun Sung**[2]***, Jong Min Kim**[1,5]***, Hyun S. Park**[1,3,6]*

Polymer electrolyte membrane unitized regenerative fuel cells (PEM-URFCs) require bifunctional porous transport layers (PTLs) to play contradictory roles in a single unitized system: hydrophobicity for water drainage in the fuel cell (FC) mode and hydrophilicity for water supplement in the electrolysis cell (EC) mode. Here, we report a high-performance amphiphilic Ti PTL suitable for both FC and EC modes, thanks to alternating hydrophobic and hydrophilic channels. To fabricate the amphiphilic PTL, we used a shadow mask patterning process using ultra-thin polydimethylsiloxane (PDMS) brush as a hydrophobic surface modifier, which can change the Ti PTL's surface polarity without decreasing its electrical conductivity. Consequently, performance improved by 4.3 times in FC (@ 0.6 V) and 1.9 times in EC (@ 1.8 V) from amphiphilic PTL. To elucidate reason for performance enhancement, discrete gas emission through the hydrophobic channels in amphiphilic PTL was verified under scanning electrochemical microscopy.

INTRODUCTION

As global warming caused by the emission of greenhouse gases becomes more serious, worldwide efforts are being made to replace fossil fuels with renewable energy. Renewable energy resources such as sunlight, wind, waves, and geothermal heat have been increasingly harvested in recent times because of their sustainability and environmental friendliness (1). However, the intermittent nature of renewable energy resources, particularly imbalances between demand and supply, has often limited their direct utilization. To solve the intermittence issue, auxiliary energy storage and conversion systems like polymer electrolyte membrane unitized regenerative fuel cells (PEM-URFCs) or Li-ion batteries have been suggested (2).

PEM-URFC is an electrochemical device that can operate in two modes of hydrogen production [electrolysis cell (EC) mode] and power production [fuel cell (FC) mode]. PEM-URFC is a hydrogen-based energy storage and conversion system, and, compared to the Li-ion battery, is superior for storing and converting large amounts of energy. Compared to Li-ion batteries, it has 5.2 times higher theoretical specific energy density (3.7 kWh kg^{-1}, in electrochemical reaction) and 4 to 10 times the packaged specific energy density (0.4 to 1 kWh kg^{-1} in the packaged system including H$_2$/O$_2$ gas tanks) (3). In addition, because the FCs and ECs are combined in a single unitized device, it has the further advantage of being a compact system with lower cost (2, 4, 5). Despite these advantages, PEM-URFC has a lower round trip efficiency than a Li-ion battery (40 to 50% for PEM-URFC; >90% for Li-ion battery) and this shortcoming remains a critical challenge to be solved. In addition, the FC and EC modes in PEM-URFC cells exhibit lower performance compared to separated single cells, and this is considered another important issue to resolve before practical application.

Among recent efforts to realize high-performance PEM-URFCs with high round trip efficiency for practical use, considerable research has been invested in the development of porous transport layers (PTLs), which are one of the key components in PEM-URFC. PTLs are critically important because they have to effectively perform contradictory roles in the EC and FC modes, and this can significantly affect the URFC performance (4, 6–12). In the FC mode, a hydrophobic PTL is needed for effective water drainage and gas-phase reactions, whereas in the EC mode, a hydrophilic PTL is more suitable to the facile transportation of aqueous reactants to the catalyst layer for electrochemical water splitting. Porous carbonaceous materials mixed with polytetrafluoroethylene (PTFE) are highly effective in the FC mode for preventing water flooding, but in the anode of PEM-URFCs in the EC mode, they are subject to severe carbon corrosion (CO$_2$ + 4H$^+$ + 4e$^-$ ⇌ C + 2 H$_2$O, E^0 = 0.206 V$_{RHE}$) due to the high potential and acidic environment (13–16).

As alternatives, Ti-based PTLs such as Ti-mesh, Ti-felt, and Ti-powders are considered promising candidates for PEM-URFCs because they provide both high conductivity and corrosion-resistant characteristics in the EC mode (6, 8–11, 17, 18). However, Ti-based PTLs often have less hydrophobicity than polymer-treated carbonaceous-based PTLs, due to the native oxide on their surface. In the FC mode, untreated Ti PTLs inevitably contribute to problematic flooding in the electrode.

Several research approaches have been suggested to achieve the appropriate properties in Ti PTLs for both the FC and EC modes of PEM-URFCs, such as coating PTFE on Ti PTLs, using a hydrophobic microporous layer (MPL) composed of Ti (9, 10), or adding graphitic carbon particles (12) to Ti PTLs. Although the addition of PTFE resin to Ti PTL improved FC performance, it adversely affected the EC mode by obstructing the transport of aqueous solution required for water electrolysis (10). An MPL composed of graphitic carbon effectively managed water distribution over the catalyst layer and enhanced the performance in the FC mode; however, it remained unstable due to carbon corrosion at high potentials in the EC mode (13, 14). Another MPL, composed of Ti particles, was difficult

[1]Center for Hydrogen, Fuel Cell Research, Korea Institute of Science and Technology (KIST), Seoul 02792, Republic of Korea. [2]School of Chemical and Biological Engineering, Seoul National University, Seoul 08826, Republic of Korea. [3]Division of Energy and Environment Technology, KIST School, University of Science and Technology (UST), Seoul 02792, Republic of Korea. [4]Green School, Korea University, Seoul 02841, Republic of Korea. [5]Materials Architecting Research Center, Korea Institute of Science and Technology (KIST), Seoul 02792, Republic of Korea. [6]KHU-KIST Department of Converging Science and Technology, Kyung Hee University, Seoul 02447, Republic of Korea.
*Corresponding author. Email: ysung@snu.ac.kr (Y.-E.S.); jongminkim@kist.re.kr (J.M.K.); hspark@kist.re.kr (H.S.P.)

to optimize with the appropriate hydrophobicity and electric conductivity while preventing native oxide formation on the small Ti particles for effective FC operation (9, 19).

Given the Janus nature of operating conditions in PEM-URFCs, the questions of whether Ti-based PTLs can simultaneously improve cell performance in both the FC and EC modes, and how to eliminate the performance trade-off in the different operations, remain unanswered. To the best of our knowledge, there have been no reports of high URFC performance with Ti PTLs that simultaneously improved the transport of gas and water in both the FC and EC modes.

Here, to improve URFC performance in both FC and EC modes, we report a high-performance amphiphilic Ti PTL fabricated with alternating hydrophobic and hydrophilic channels by selective surface modification. In this process, hydroxyl-terminated polydimethylsiloxane polymer (PDMS brush), which is a well-known inherently hydrophobic material, is covalently attached to hydrophilic Ti surface at regular intervals for construction of the defined hydrophobic and hydrophilic channels (20–23). To create the hydrophobic and hydrophilic networks, a patterning process was performed using a spraying-coating method with a shadow mask, known as shadow mask patterning, which has the advantage of low cost and large area coverage. The resulting amphiphilic Ti PTLs provided enhanced mass transport characteristics for both FC and EC operation, i.e., hydrophobic and hydrophilic channels for effective gas and water transport, respectively, enabling stable and high performance of PEM-URFCs with a low amount of noble metal catalysts.

RESULTS AND DISCUSSION
Amphiphilic PTL fabrication
The patterned hydrophilic/hydrophobic channels on the surface of Ti PTLs were constructed by selectively depositing a hydrophobic polymer solution on the hydrophilic Ti PTL. Among many hydrophobic polymers, the hydroxyl-terminated PDMS brush was used in this study. It firmly and covalently links to the metal oxide surface via a condensation reaction between the functional hydroxyl end groups of the PDMS brush and the hydroxyl groups on the metal surfaces. The thickness of the tethered PDMS brush film was controlled to be nanometer thin (1 to 100 nm) depending on the molecular weight (MW) of the polymer, and this was sufficient to control the surface polarity of PTL, from hydrophilic to hydrophobic, after simple solution impregnation and thermal annealing steps (20, 24–26). The unique properties of PDMS, such as thermal and oxidative durability, high gas permeability, and chemical inertness, also ensured the operating stability of PEM-URFCs under harsh oxidative conditions (27).

A patterned shadow mask was used to confine the hydrophilic and hydrophobic area of the Ti PTL electrode (Fig. 1). The use of a patterned shadow mask, i.e., mechanical aperture plates, has the advantages of low cost and simple process when making a micropattern over large surfaces. To define the hydrophilic and hydrophobic patterns on one side of Ti PTL (the top side of PTL), a P4VP homopolymer solution was spray-coated through shadow masks with a large pattern (LP; pitch, 250 μm; width, 125 μm) or small pattern (SP; pitch, 75 μm; width, 30 μm). In this way, P4VP-coated and noncoated areas were alternately formed (Fig. 2 and fig. S1).

Top-view scanning electron microscopy (SEM) and energy dispersive x-ray spectroscopy (EDS) images of the P4VP-coated LP PTL confirmed that the P4VP-coated region (hydrophilic region) had the intended periodic morphology produced by the shadow masks (Fig. 2). On the opposite side, the entire surface was first covered by electrodeposited IrO_2 (e-IrO_2) followed by a hydrophilic P4VP homopolymer coat (Figs. 1 and 2E). e-IrO_2 was used as the active oxygen evolution reaction (OER) catalyst for EC operation and was protected by sprayed P4VP solution before the PDMS coating was applied (28,29). e-IrO_2 layered on Ti PTL (thickness, ~180 nm) creates hydrophilic catalyst surfaces for facile water transport and high electrolysis performance using a low amount of catalysts (~0.15 mg cm^{-2}) without using ionomers (29). Because of the large difference in Hildebrand solubility parameter between P4VP (δ ~ 23.0 MPa$^{1/2}$) and the heptane solvent (δ ~ 15.3 MPa$^{1/2}$), which is a good solvent for the PDMS brush, P4VP effectively preserved the e-IrO_2 surface of PTL during the PDMS brush covering process (23, 30). Unlike the PDMS brush with reactive hydroxyl functional groups, the P4VP homopolymer does not chemically react to the Ti PTL surface; thus, it can be simply removed by IPA (isopropyl alcohol) washing when necessary. The P4VP film acts to prevent coating with the PDMS brush, and it turns into a conductive hydrophilic electrode when P4VP is removed in the washing process.

A cross-sectional EDS mapping image confirmed that approximately 30- and 50-μm thickness of PTL was covered by P4VP on the bottom-side and top-side channels, respectively (Fig. 2). After that, the PDMS brush solution was impregnated to the electrode and thermally annealed to covalently link the PDMS brush to the Ti PTL surface. In the thermal treatment, the hydroxyl end groups of the PDMS brush react to hydroxyl groups on the Ti surfaces, establishing a strong covalent bond through a condensation reaction. Last, the unattached PDMS and P4VP homopolymer were washed off with heptane and IPA solvents, respectively. Consequently, Ti PTLs without treatments [pristine PTL (PS)], with a nonpatterned PDMS brush layer (NP), and with small (SP) and large patterned PDMS area (LP) were prepared.

The surface polarity of the four different electrodes (PS, NP, SP, and LP) was investigated by observing absorption of a water droplet on the top surface of Ti PTLs using optical microscopy (OM) images and photographs (Fig. 3, A and B). The top surface of PS exhibited a super hydrophilic surface, and the water droplets rapidly disappeared when dropped. As a result, a substantial amount of water was accumulated in the PS bulk. The water contact angle of PS PTL was practically 0° (Fig. 3C, left). In contrast, the NP PTL presented hydrophobic surfaces with a contact angle of 145°, demonstrating that the polarity was modulated to hydrophobic surfaces by the PDMS brush layer (Fig. 3C, right). As intended, SP and LP PTLs, which have both hydrophilic/hydrophobic domains, showed clearly visible wet-stripe micropatterns as the water droplets fell on the surface. The stripe patterns where the water tended to accumulate well matched the size of the hydrophilic domains (marked by blue channels, as shown in Fig. 3, A and D). Meanwhile, the PDMS brush–treated region (marked by red channels in Fig. 3, A and D) exhibited water-resistant properties as shown in SP and LP PTLs. The clear contrast of wet-and-dry stripes on LP PTL proved that amphiphilic patterns were successfully formed on the PTL surface by the patterning process (Fig. 3D).

The electrical conductivity of the PDMS-treated and untreated Ti TPL was measured by four-probe method (fig. S2). Sufficient electric conductivity is essential for components in electrochemical devices. PS and NP PTLs exhibited conductivities of 8.5×10^5 and 5.6×10^5 S/m, respectively, so only an insignificant ohmic voltage
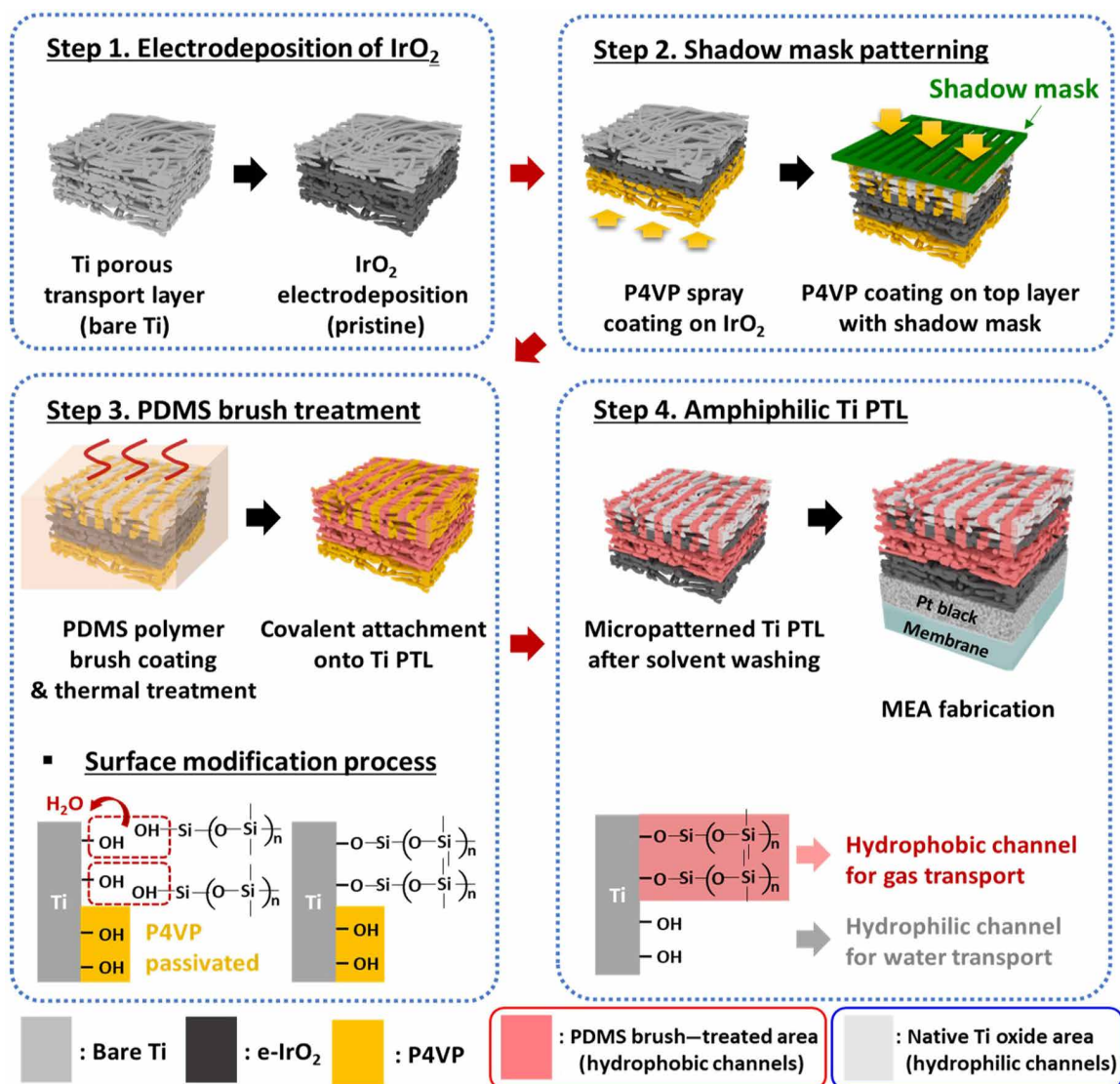
Fig. 1. Schematic fabrication procedure of the amphiphilic Ti PTLs.

loss was expected from both electrodes. Although the PDMS brush is an electrical insulator, the electrical conductivity of NP was found to be similar to the bare PTL. This is due to the ultrathin layer (2 nm) of the tethered PDMS brush layer on the NP surface (*20*). In summary, surface modification with the PDMS brush successfully changed the surface polarity of Ti PTLs without significantly compromising their electrical properties.

Because the PDMS brush alternately contains silicon and oxygen atoms in its backbone, it is possible to confirm whether the PDMS brush treatment was successfully performed by checking for the presence of Si 2p peaks. From the x-ray photoelectron spectroscopy (XPS) spectra of the Si 2p peaks, it was confirmed that the PDMS brush was covalently linked to the top surface of the NP PTLs, while the IrO$_2$ surface was free of PDMS, as intended (Fig. 3E). A high-intensity Si 2p peak was observed at the top surface of NP PTL in contrast to that of PS, confirming that the PDMS brush was successfully applied to the NP surface. However, no Si 2p peak was detected from the IrO$_2$ side of the NP PTL, which indicates that the P4VP

homopolymer layer protected the surface of the electrodeposited IrO$_2$ well during the PDMS brush treatment, as designed.

In addition, the presence of PDMS on the NP PTL was confirmed from the carbon K-edge near-edge x-ray absorption fine-structure (NEXAFS) spectra of PS, NP PTLs, and the PDMS brush (Fig. 3F). The spectra of pristine PDMS have been reported with emissions from the σ* C—Si bonds centered at 291 eV, and σ* C—H in the vicinity of 287.4 eV (*31*, *32*). As reported in the literature, intense σ* C—Si emissions at 291 eV and of σ* C—H at 287.4 eV were observed for the PDMS brush, and NP PTL also exhibited those absorbance bands for σ* C—Si and σ* C—H at the same position. The overall shape of the NEXAFS spectra for NP PTL showed patterns similar to those of PS PTL, in addition to the PDMS footprint, once again proving that the PDMS brush was tethered to the surface of Ti PTL.

FC operation of URFC
The four types of PTLs (PS, NP, SP, and LP) were sequentially used as the oxygen electrode of a single URFC device. In the oxygen electrode
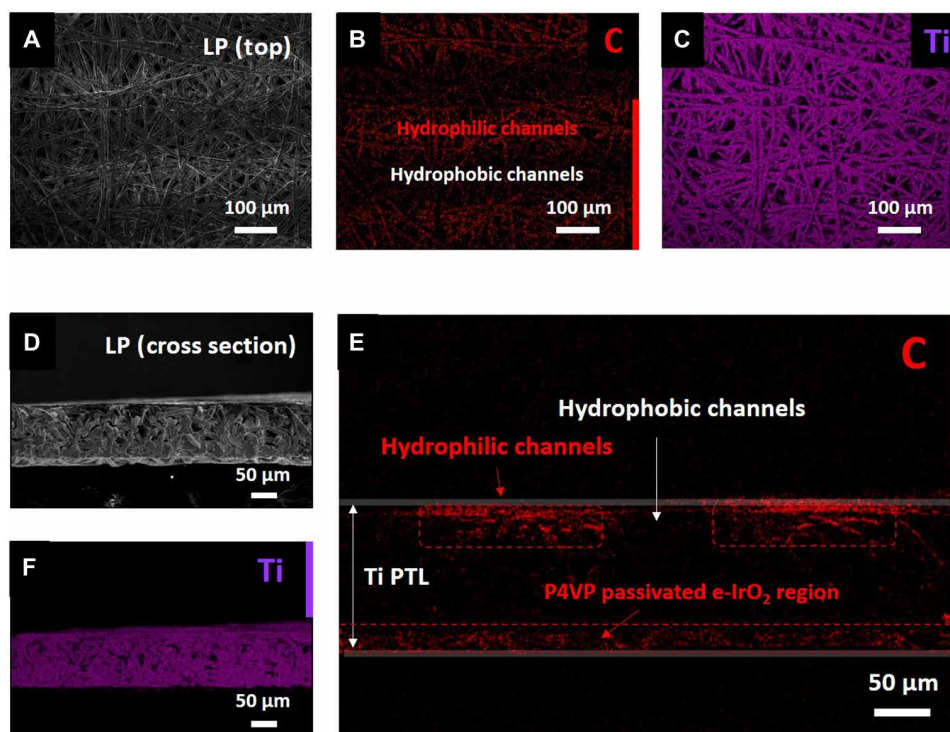
Fig. 2. SEM and EDS analysis of the amphiphilic Ti PTL. (**A**) Top-view SEM image of LP PTL (after the P4VP patterning process using a shadow mask and before PDMS polymer brush coating process). The opposite side of all samples was coated with IrO_2 through electrodeposition. (**B** and **C**) Corresponding EDS mapping (top) results for carbon, titanium elements. (**D**) Cross-sectional SEM images of LP PTL (after P4VP patterning process using a shadow mask). (**E** and **F**) Corresponding EDS mapping (cross section) results for carbon and titanium elements. The red dashed lines are guide to the eye, indicating the coated area of P4VP homopolymer after the spraying process.

of URFC, e-IrO_2 formed on Ti PTL and Pt sprayed on the ion-conducting membrane were used together for OER and oxygen reduction reaction (ORR), respectively, for EC and FC operation.

In the FC mode, the facile transport of oxygen to the Pt surface is important for efficient ORR, with higher mass transfer limited current (*33*). However, the Pt layer in a conventional URFC oxygen electrode makes direct contact with the hydrophilic e-IrO_2 catalysts, and the water present in the cathode can be trapped at the interface of Pt and e-IrO_2. This impedes oxygen transport through the junction to the Pt surface. The water in the cathode is either produced by ORR, dragged by electro-osmosis from the anode, or supplied as steam in the oxygen gas.

When the Pt surface is flooded by an excessive water layer, oxygen concentration can be dropped to 0.2 to 0.7 mM [the saturated concentration at 333 to 363 K in aqueous solution (*34*)] at the catalyst surface (FC mode of PS PTL in Fig. 4A). The cell using PS actually showed degraded FC performance in RH 65 with a maximum power density of less than 70 mW cm^{-2} (black solid line, Fig. 4B). In addition to limiting mass transport, excess water in the FC cathode induces an adverse increase in ohmic resistance by the back diffusion of water to the anode side through the membrane. The water diffusion from cathode to anode counteracts the solvated proton transfer from anode to cathode, increasing ohmic resistance, especially under low RH conditions (*35*). Here, ohmic resistance in the PS cell was measured to be more than two times higher compared to those using other PTLs, e.g. 0.54 and 0.24 ohm·cm^2 for PS and LP, respectively.

However, when PTLs with controlled amphiphilic channels were used, the water flooding in the oxygen electrode was modulated.

The flooding of the oxygen electrode was enormously ameliorated during FC operation, as manifested by the *I-V* curve obtained with RH 65 oxygen gas (Fig. 4B), when the hydrophobically treated NP, SP, and LP were used on PTLs.

For example, the cell with NP, which had the most hydrophobic surfaces among the prepared PTLs, achieved a 2.8 times higher current density at 0.6 V_{Cell} compared to the untreated PS. However, the maximum current density of NP at lower voltages was still limited to a current density less than 1.0 A cm^{-2}, implying that voltage loss was still occurring in the cathode due to mass transport limitation. The current densities with the amphiphilic PTLs, i.e., SP and LP, at 0.2 V_{Cell} outperformed the NP cell. The cells with SP, LP, and NP exhibited 1.0, 1.7, and 0.75 A cm^{-2}, respectively. Furthermore, the FC performance with LP exceeded that of both SP and NP over all current and potential ranges, as shown in Fig. 4B. The more significant enhancement of performance in LP compared to SP appears from the higher hydrophobic portion in patterning of LP (LP, 50%; SP, 40%). These results imply that the water and gas channels, formed by the presence of distinct hydrophilic and hydrophobic regions in a single PTL, enhanced FC performance by appropriately managing water in the cathode catalyst layer (FC mode of patterned PTL in Fig. 4A).

The effect of the amphiphilic PTLs during FC operation was more remarkable when fully hydrated gas, i.e., RH 100 oxygen gas, was supplied to the cathode. Because the intentional inflow of excess water to the cathode causes flooding problems, the absolute current and power densities of all samples tested with RH 100 oxygen gas decreased to less than 50% of those obtained with the RH 65 oxygen gas. PS and NP had no practical power generation under the
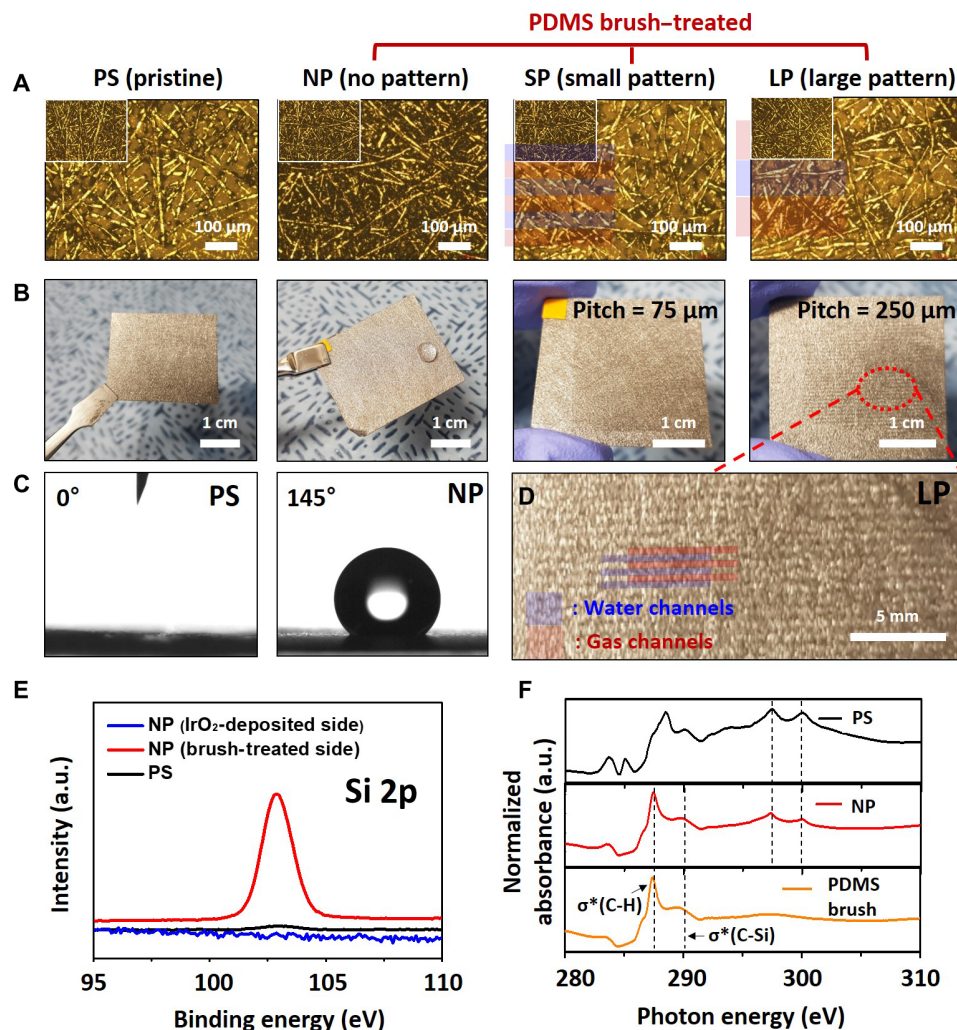
Fig. 3. Surface characterization of electrodes. (**A**) OM images of PS (pristine), PDMS polymer brush–treated NP (no pattern), SP (pitch, 75 μm), and LP (pitch, 250 μm) after dropping water. The upper inset shows the corresponding OM images before dropping water. (**B**) Photographs of PS, NP, SP, and LP after dropping water. (**C**) Water contact angle images of PS and NP. (**D**) An enlarged photograph of LP. (Blue indicates the region of hydrophilic channels, and red indicates the region of hydrophobic channels.) (**E**) Surface characterization of Si 2p by XPS on the surface of the IrO_2-electrodeposited NP (bottom side), brush-treated NP (top side), and PS (top side) PTLs. a.u., arbitrary units. (**F**) NEXAFS C K-edge spectra of PS, NP, and hydroxyl-terminated PDMS polymer brush.

fully humidified gas, because the inefficient water management obviously deteriorated the FC reactions.

However, SP and LP displayed meaningful power densities of approximately 0.1 W cm^{-2} even under these severe operating conditions (Fig. 4C). The results measured under intentional flooding conditions suggest that the amphiphilic channels of PTLs facilitate the transport of gas and water in discrete ways, as in the cells with SP and LP. The maximum power density of 391 mW cm^{-2} was achieved in LP, a 3.4 times increase compared to PS (RH 65). LP produced a clear improvement in FC operations compared to PS and NP under different RH conditions, which strongly illustrates the constructive effect of the amphiphilic PTL channels on the mass transport of water and oxygen in the FC cathode.
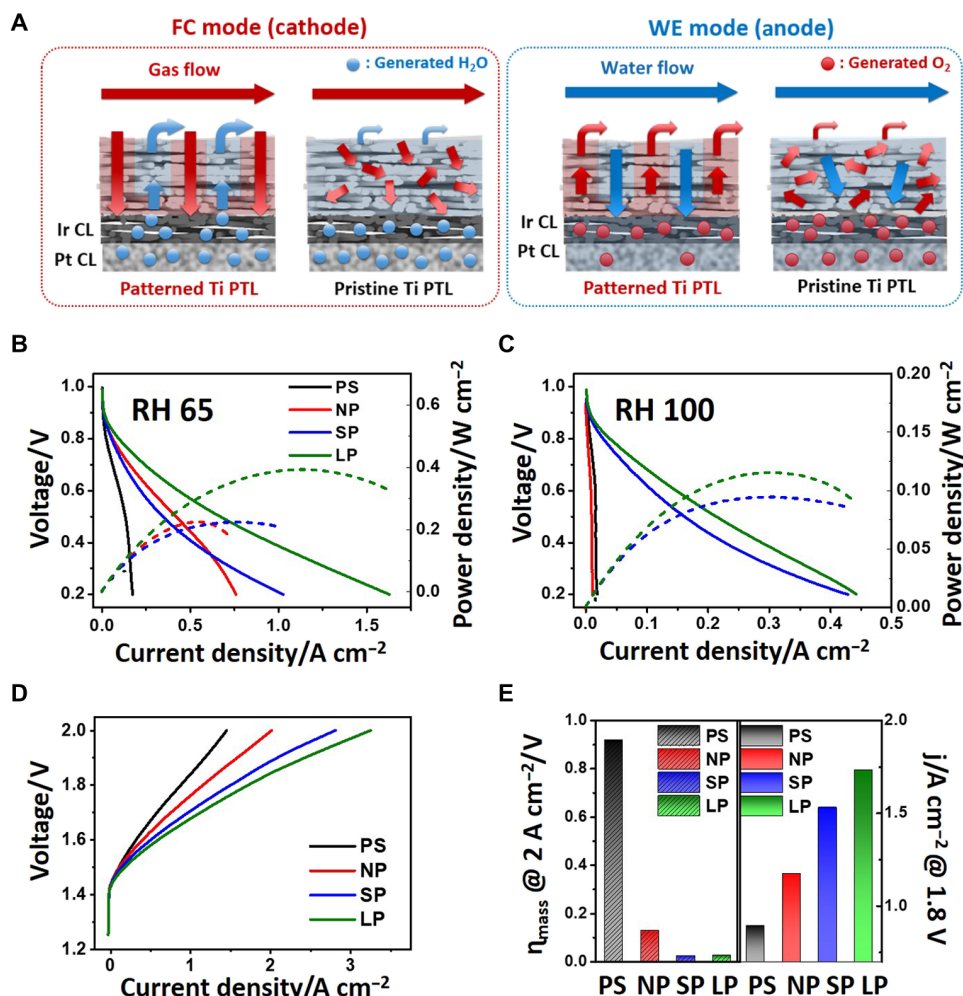
EC operation of URFC

EC operation is just the opposite of FC operation, because it requires a sufficient inflow of water to the catalyst surface as well as the facile removal of gas product. Water electrolysis efficiency is often reduced by using hydrophobic PTL because it obstructs the mass transport of water needed for EC operation (10). Also, stagnated water trapped in the catalyst layer prevents the elimination of gas bubbles attached to the active surfaces (36).

Among the different PTLs using the hydrophilic e-IrO_2 electrode, EC performance was poorest on PS. It displayed a current density of 1.4 A cm^{-2} at 2 V_{Cell}, while other cells using the PDMS-treated PTLs showed improved current densities, of more than 39% at 2 V_{Cell} (Fig. 4D). Beginning with the untreated PTL, EC performance increased in the order of NP < SP < LP cells, with 2.0, 2.8, and 3.2 A cm^{-2} at 2 V_{Cell} for NP, SP, and LP, respectively (Fig. 4D).

The Pt layer inserted in between e-IrO_2 and the ion-conducing membrane was found to be a significant determining factor on the EC performance of the PS cell (black and pink curves in fig. S3). When the cell using PS was constructed without the Pt layer, the performance increased by more than 100% compared to PS with the Pt layer, so it actually performed similar to the best URFC device, i.e., LP. The EC performance of PS increased from 0.9 to 1.7 A cm^{-2}

Fig. 4. Schematic mass flow and electrochemical analysis in the FC and EC mode of URFC operation. (**A**) Schematic diagram of mass transfer pathways in the patterned (left) and pristine (right) Ti PTL under FC and EC modes. The red arrows indicate the diffusion path of the oxygen, and the blue arrows indicate water entering the electrode. (**B** and **C**) Comparison of I-V performance and power density for PS, NP, SP, and LP in the FC mode at RH 65 and RH 100. (**D**) Comparison of I-V performances of PS, NP, SP, and LP in the EC mode. (**E**) Comparison of overvoltage from mass transport limitation resistance at 2 A cm^{-2} and current density at 1.8 V for PS, NP, SP, and LP.

at 1.8 V_{Cell} when the Pt layer was removed from PS. Pt catalyst layers, used in the ORR electrode for FC operation, have long been optimized for facile gas permeation while retaining a small amount of water in the polymeric ionomers for ion conductivity. Because the ORR electrode has a porous structure for gaseous reaction, (i) the hydrophobic Pt layer prevents sufficient water from reaching the Pt and e-IrO$_2$ interface while (ii) capturing the oxygen gas produced from OER at the junction, so it hinders the EC reaction. In addition, (iii) the adjacent Pt catalyst layer can block part of the e-IrO$_2$ surface at the interface, further reducing the e-IrO$_2$ active surface area for OER.

In other words, the very property that is indispensable for active FC operation has a negative influence during electrolysis. This negative effect involves three main aspects, as compared to the case without Pt catalysts. Ohmic and charge transfer resistance increased from 0.14 to 0.17 ohm·cm^2 and from 0.02 to 0.04 ohm·cm^2, respectively, by inserting the Pt catalyst layers between e-IrO$_2$ and the ion-conducting polymer. This demonstrates the important effect of water and oxygen transportation on both ohmic resistance and charge transfer resistance. However, the use of a Pt catalyst in the oxygen electrode is essential for FC operation in URFC.

Here, the controlled polymer brush coating on PTL was found to ameliorate the inevitable negative effects of the Pt catalyst layers on the e-IrO$_2$ electrode. It seems that the amphiphilic PTLs appropriately modulate the water inflow and enhance the oxygen outflow at the PTL layer, effectively reducing the oxygen gas present inside the catalyst layer of e-IrO$_2$ and Pt (EC mode of patterned PTL in Fig. 4A). By mitigating the oxygen concentration trapped in the catalyst layer, the electrode using SP and LP PTLs recovered the OER performance at e-IrO$_2$ even when a Pt catalyst layer was present in the URFC electrode (Fig. 4D).

The EIS spectra shown in fig. S4 indicate a clear reduction in charge transfer and ohmic resistance for the LP and SP electrodes, compared to the untreated PTL or NP electrodes. In other words, the EC performance of the Pt/e-IrO$_2$/PTL electrode was greatly enhanced when the patterned PTLs behaved as controlled pathways for water and gas transportation. Comparing PS and optimized LP, overvoltage from the mass transport limitation decreased significantly at 2 A cm^{-2}, while the current density at 1.8 V improved 1.9 times during EC operation (Fig. 4E) (37). In addition, the ohmic resistance of PS was observed to be about 1.5 times higher than that

of LP, which is believed to be due to the entrapped O_2 in the Pt layer during the high-current EC operation with sluggish mass transport through PS PTL. The gas bubbles block the pores and reduce the aqueous electrolyte content between the catalyst layer and ion conduction membrane, resulting in the high ohmic resistance.

The enhanced transport of gas bubbles by the patterned PTLs during OER was also visually confirmed using a liquid half-cell system (Fig. 5). Typically, oxygen bubbles are generated at the surface of the IrO_2 during OER and then escape through the porous PTL. Under a constant oxygen bubble production rate, i.e., at the same current density, relatively large bubbles are formed at the hydrophilic PS PTL, whereas only small bubbles were seen for the amphiphilic LP PTL (Fig. 5, B and C). The visual observation of bubble growth and removal on PS and LP PTL demonstrates the advantages of the amphiphilic channels on the patterned PTL for the facile mass transportation of water and gas.

It seemed that the growth and detachment of small oxygen bubbles was faster via the hydrophobic channels of LP, while both large and small bubbles were observed on the PS surface, with slow bubble detachments. Obviously, because the amphiphilic patterned surface of LP has clear and separate pathways for gas and water, as confirmed by the visual observation, the oxygen concentration over the PTL surface should be modulated by the polymer patterns. An uneven distribution of oxygen close to the PTL surface, less than the diffusion layer thickness, was further demonstrated using the scanning electrochemical microscopy (SECM) technique (see below), confirming that the efficient transport of oxygen bubbles was the reason for the excellent URFC performance. However, the thickness

of amphiphilic pattern was fixed at approximately 50 μm in this study. The penetration depth of the amphiphilic channels can also be optimized by further controlling the spraying pressure and the amount of polymer solution in the fabrication process, and there is room for further improvement of the URFC performance.

Oxygen distribution studied by SECM
Both the FC and EC performance of URFC were improved by application of the PDMS brush patterned PTLs, as shown above. The rapid growth and detachment of oxygen bubbles during EC operation imply the facile mass transportation of water and oxygen through the patterned PTLs. The visual observation of the oxygen bubble formation on LP PTL also indicated the separated pathways for oxygen gas and water through the patterned surface. To quantify the controlled transportation of oxygen gas over the patterned PTL, the substrate generation/tip collection (SG/TC) mode of SECM was used. Briefly, a Pt ultramicroelectrode (UME) of 25 μm diameter was placed on the top patterned surface of LP, and 1.15 and 0.0 $V_{Ag/AgCl}$ were applied to LP and UME, respectively, for OER and ORR. Then, the oxygen generated and released from LP was detected by Pt UME (SG/TC mode of SECM). Because Pt UME is located near the surface in the diffusion layer, at a distance of approximately 30 μm, any oxygen local concentration changes above the PDMS pattern (LP, pitch, 250 μm; width, 125 μm) can be detected by UME (Fig. 5, D to F).

To bring UME to the LP surface, the surface morphology of Ti PTL was first examined using a $[Fe(CN)_6]^{3-/4-}$ redox couple. Figure S5A shows the line scan profile over Ti PTL using the negative and positive feedback modes of SECM (blue and orange lines in fig. S5A,
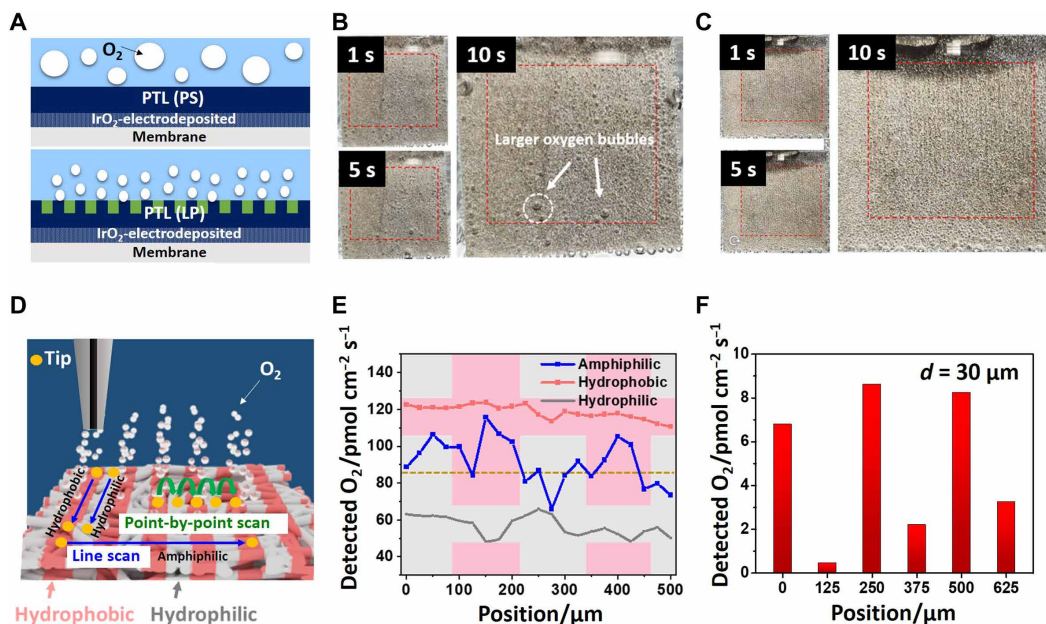
Fig. 5. Schematic illustration, photographs of bubble emission in PS and LP, and verification of selective bubble emission in LP by SECM. (A) Schematic illustration during the oxygen evolution reaction in the liquid half-cell system. **(B)** Photography of the top side of hydrophilic PS (pristine) PTLs during OER (@ 20 mA cm^{-2}). The area of the red square is 5 cm^2, which is the patterned area in (C) compared to (B). **(C)** Photography of the top side of LP PTLs during OER (@ 20 mA cm^{-2}). A Nafion membrane was attached to the bottom side of PTLs through hot press so that the generated O_2 gas could only move through the top side of PTLs. **(D)** Schematic illustration of the line scan and point-by-point measurement of the OER-ORR (SG/TC) modes of a UME on the top side of LP. The line scan was measured along the hydrophilic, hydrophobic, and amphiphilic directions. For the point-by-point measurement, the hydrophilic and hydrophobic channels were measured alternately. **(E)** Detected O_2 through the line scan on the top side of LP along the amphiphilic, hydrophobic, and hydrophilic channel directions. Potentials of the substrate and the tip were 1.15 $V_{Ag/AgCl}$ and 0 $V_{Ag/AgCl}$ in the OER-ORR (SG/TC) modes. **(F)** Detected moles of oxygen on the UME tip on each position of the top side of LP (d = 30 μm) in the point-by-point measurement.

respectively). The results indicate the surface roughness of Ti PTL with empty pores between Ti wires. The line mapping above the top surface of Ti PTL was conducted with an average tip-substrate distance (d) of 17 μm. A two-dimensional (2D) scan performed on Ti PTL also revealed a random network of Ti fibers (500 μm × 500 μm, tip @ −0.25 $V_{Ag/AgCl}$, PTL @ 0.6 $V_{Ag/AgCl}$, d = 24.5 μm; fig. S5B). The SECM image displays the Ti-felt surface consisting of tangled Ti fibers with approximately 20 μm diameters, which coincides with the OM and SEM images of PTL (Fig. 3A and fig. S6).

In the analysis of oxygen distribution by SECM, the oxygen bubbles evolved by OER at the e-IrO_2 layer are transported and released to the bulk solution through the patterned side of PTL. Pt UME placed close to the PTL surface was at 0.0 $V_{Ag/AgCl}$ for ORR, while the potential to LP PTL was set at 1.15 $V_{Ag/AgCl}$ for OER in 0.5 M Na_2SO_4 aqueous solution (Fig. 5, D to F). Note that the appropriate distance between Pt UME and Ti PTL is far enough to avoid confining the gas bubbles, but not so far that it decreases the collection efficiency of the SG/TC mode of SECM. In fig. S7, the collection efficiency, i.e., the ratio of detected amounts of electroactive species at UME to that produced at the substrate, obtained in the OER/ORR mode of SECM, was compared to the positive feedback of SECM measured using the $[Fe(CN)_6]^{4-}/[Fe(CN)_6]^{3-}$ redox couple. The normalized oxygen collection efficiency measured at d = 17 μm indicates that the oxygen concentration is higher above the pore region and lower when the Ti fiber blocks the oxygen transportation from e-IrO_2 at the bottom of Ti PTL. However, the morphology effect was reduced at d = 27 μm with a slightly decreased, but reasonable, oxygen collection efficiency. The effect of the patterned PTL on the local oxygen concentration was measured at d = 30 μm, and the PTL morphology was found to not have a significant effect on the measurements.

In the SECM measurement scanned perpendicular to the polymer pattern direction, the local O_2 flux released from the LP electrode exhibited a fluctuation pattern with approximately 125 μm between the maximum and minimum flux from the SECM measurements, or a peak-to-peak distance of approximately 250 μm (Fig. 5, E and F). For example, an O_2 flux of more than 100 pmol cm^{-2} s^{-1} was observed at two peak points above the 400-μm line scan of Pt UME, whereas a reduced O_2 flux was observed in between the maximum points. The highest and lowest O_2 flux was 117 and 65 pmol cm^{-2} s^{-1}, respectively, at a 125-μm distance from each other, implying that there was discrete O_2 distribution over the amphiphilic channels of LP PTL. When UME moved parallel to the hydrophobic or hydrophilic channel, relatively steady O_2 flux mean values of 120 and 58 pmol cm^{-2} s^{-1}, respectively, were detected.

A similarly uneven O_2 distribution was double-checked by a point-by-point measurement in Fig. 5F. In the measurements, UME was stationed at each different point, a potential pulse was applied to the LP electrode for 10 s, and the ORR current was measured at Pt UME (fig. S8). Using the SG/TC mode of SECM with the potential step, the background current at the tip can be subtracted from the signal at each point. In the potential step measurements, the detected O_2 flux at Pt UME also showed an obvious up-and-down pattern with a point-to-point distance of 125 μm (Fig. 5F). The high and low O_2 flux over the point detection was more than twice as different in the range from 0.5 to 8.6 pmol cm^{-2} s^{-1}.

In addition to using the SG/TC mode of SECM at the actual oxygen electrode, an identical experiment was conducted in a model system to validate the SECM measurements on the LP electrode.

The model study was done using 1.2 mM $[Fe(CN)_6]^{3-}$ redox couple released from a circular hole with a diameter of 250 μm (fig. S9). The concentration $[Fe(CN)_6]^{3-}$ was chosen to simulate the saturated O_2 in aqueous solution, so the UME current detected over the pinhole showed the simulated O_2 concentration at d = 30 μm as it diffused from the saturated O_2 source (34). The measurement was also performed on a flat surface so that the UME current was not affected by any surface roughness.

The ratio of signal current to background level was more than three times over a 500-μm scan, so the highest and lowest $[Fe(CN)_6]^{3-}$ flux were calculated to be 132 and 40 pmol cm^{-2} s^{-1}. The flux decreased from 132 to 92 pmol cm^{-2} s^{-1}, while UME moved 250 μm from the center of the hole to the inert surface, which is similar to the maximum-to-minimum flux changes detected over the LP electrode (125/250 μm: pattern width/pitch). The results of the model study also validated the measurements of the actual LP electrode used to determine the local O_2 flux (also see the Supplementary Materials for experimental details).

The results of the nonuniform and delocalized high and low O_2 flux measurements repeated with an average distance of 125 μm strongly indicate the intended gas removal mainly through the hydrophobic channel produced in LP. The optical images obtained from the liquid half-cell operation (Fig. 5C) also show that small-sized O_2 bubbles generated at LP were released through the patterned LP due to facile detachment of O_2, while large bubbles formed and attached to the hydrophilic surface of the untreated Ti PTL. The SECM results obtained for the line and point detection confirm that the generated gas bubbles are transported through the patterned hydrophobic channels fabricated with the PDMS polymer brush coat.

Round trip operation of URFC

The EC and FC performances of PEM-URFCs were summarized for the different Ti PTLs used in the oxygen electrode (Fig. 6A). Round trip efficiency (RT), the cell voltage ratio at a particular current density for both the FC and EC operations, was enhanced from 0 to 27% @ 0.5 A cm^{-2} by the hydrophobic treatment (PS versus NP). Furthermore, LP with the appropriate pattern channel fabricated in PTL achieved the highest RT among the cells studied, which was 36% @ 0.5 A cm^{-2} (inserted in Fig. 6A).

In previous reports, a high RT is often achieved by using an excess amount of precious metal catalyst (Fig. 6B) (5, 6, 10, 38–42). It is partially due to the low catalyst utilization of powdery catalysts used in URFC with severe catalyst agglomeration, electrical disconnection by ionomeric binder, inappropriate porosity of catalyst layer, etc. (43, 44). For instance, Grigoriev et al. (38) achieved a 31% RT with 2.8 mg$_{(Pt+Ir)}$ cm^{-2} of noble catalysts. Ioroi et al. (10) reported outstanding RT of 46.5% using hydrophobic Ti PTL, but large quantities of catalysts (6 to 8 mg cm^{-2}) were used. e-IrO_2 (<200 nm on Ti fibers) was used to increase the catalyst utilization in URFC with enhanced electrical connection between catalyst and electrode support without using ionomers (28, 29). However, as shown in this study, the coexistence of hydrophobic Pt catalysts and hydrophilic e-IrO_2/Ti PTL negatively influences each other in FC and EC operation, and the amphiphilic treatment on e-IrO_2/Ti PTL improves RT from 0 to 36% (@ 0.5 A cm^{-2}) by solving mass transport limitation. It indicates that several factors including the catalyst preparation method, loading amount, the selective control of surface hydrophobicity of Ti PTL (amphiphilic PTL), and many others are important for the URFC efficiency.
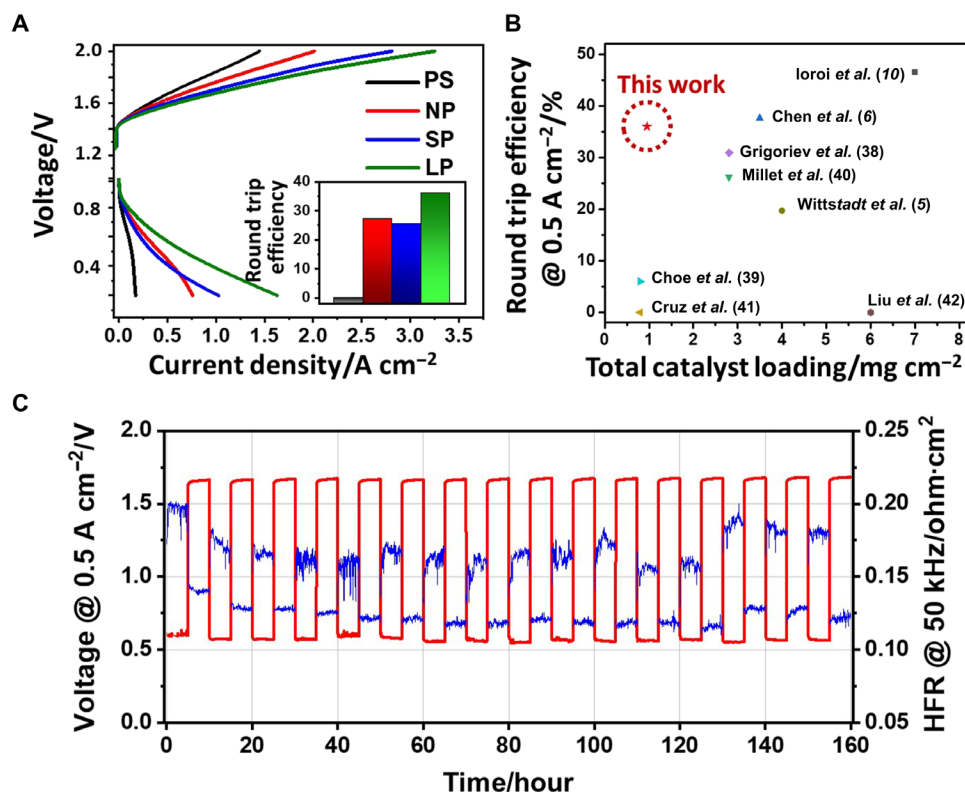
Fig. 6. URFC performance and durability test. (**A**) URFC performance and round trip efficiency (RT) at 0.5 A cm^{-2} of PTLs (PS, NP, SP, and LP). (**B**) Comparison of RT at 0.5 A cm^{-2} versus total catalyst loading in a URFC single cell from previous studies. The data of previous studies in the graph are limited to the case with noncarbon PTLs in the oxygen electrode of URFC. (**C**) Long-term URFC operation of LP at 0.5 A cm^{-2} (FC: H$_2$/O$_2$, RH 65). During long-term operation, high-frequency resistance at 50 kHz in Galvanostatic Electrochemical Impedance Spectroscopy (@ 0.5 A cm^{-2}) was measured every 2 min.

Consequently, high RTs of 49 and 36%, respectively, were accomplished at 0.4 and 0.5 A cm^{-2} using only 0.95 mg$_{(Pt+Ir)}$ cm^{-2} of noble catalysts by surface engineering of Ti PTL. It is attributed to both high catalyst utilization of e-IrO$_2$ and the significant enhancement in mass transport for both the FC and EC operations, when the amphiphilic PTL was used as the substrate of oxygen electrode in PEM-URFC.

Last, the stability of URFC and the patterned Ti PTL was confirmed in a durability test @ 0.5 A cm^{-2} for 160 hours. The durability test consisted of 16 cycles of FC and EC operations, where each FC or EC operation was performed for 5 hours. When LP PTL was used in the oxygen electrode, the URFC device performed well in the cycle test, exhibiting degradation rates of 632 and 614 μV hour^{-1} for the FC and EC modes, respectively (Fig. 6C). The average cell voltages for FC and EC operation at 0.5 A cm^{-2} were 0.6 and 1.7 V$_{Cell}$, respectively. Of particular interest, no sudden decrease in FC performance was observed during the 160 hours, as had been reported in a previous study (29), and no increase in ohmic resistance. The ohmic resistance measured at 50 kHz remained in the range from 0.1 to 0.2 ohm·cm^2.

The main cause of performance degradation was found to be the increase in kinetic resistance, probably due to the dissolution, migration, and coalescence of the catalysts in the severely reductive and oxidative cycle operation (45–47). Increase of Rct (charge transfer resistance) in FC operation and 31% reduction of electrochemical active surface area (ECSA) of Pt calculated by Hupd (from 27.2 to 18.7 m^2 g^{-1}$_{Pt}$) were confirmed after 160-hour operation (fig. S10, A and B). da Silva et al. (46) recently reported the significant dissolution of Pt during repetitive ORR-OER cycles of URFC. The degradation rate of FC and EC operation was similar to each other, for 632 and 614 μV h^{-1}, respectively, in the durability test. It indicates that both Pt and IrO$_2$ were damaged in the repeated FC and EC cycles. In Nyquist plots obtained at 1.5 V, where the kinetic of OER catalyst dominates EC performance, Rct was significantly increased from approximately 0.38 to 0.63 ohm·cm^2 (fig. S10C). It implies that the repeated FC and EC operation obviously degraded the OER catalyst. However, EC current reduction at 1.7 V, where the mass transport resistance is also largely involved, was approximately 10% during the durability test (fig. S10D). Thus, it is speculated that the main cause of URFC performance loss was the degradation of ORR and OER catalyst.

To enhance the stability of the URFC device, the use of more stable Pt on corrosion resistive supports, e.g., Pt/SnO$_2$ (48), a Pt monolayer on CeOx (49), robust OER catalysts, and a reinforced membrane with good thermomechanical stability (50, 51), should be applied in PEM-URFC. However, despite the 31% reduction in Pt ECSA, an RT of 33% was recorded after 160 hours of operation, which was only 3% less than the initial RT of the fresh cell. In summary, an amphiphilic Ti PTL for efficient URFC operation with patterned hydrophilic and hydrophobic channels is first introduced in this study. The patterned PTL was designed with optimized water and gas transportation pathways, simultaneously fulfilling the contradictory

requirements of PTLs for PEM-URFC, namely, hydrophobic properties for efficient FC operation and hydrophilicity for active EC operation. In the oxygen electrode of a conventional PEM-URFC, hydrophilic IrO_2 catalysts and hydrophobic Pt catalysts become disrupters in the FC and EC modes, respectively. By introducing facile water and gas transport, the amphiphilic PTL improved URFC performance 4.3 times in the FC mode (@ 0.6 V, RH 65) and 1.9 times (@ 1.8 V) in the EC mode compared to the device using pristine Ti PTL. With the amphiphilic Ti PTL, an RT of 36% was achieved using only 0.95 $mg_{(Pt+Ir)}$ cm^{-2}. The preferred path of gas emissions through the hydrophobic pathways of the amphiphilic Ti PTL was verified by measuring the uneven distribution of the O_2 flux over the patterned Ti PTL in the SG/TC mode of the SECM technique. The stability of the amphiphilic Ti PTLs was further demonstrated during 160-hour long-term operation in URFC. We believe that the approach shown in this study provides valuable insights that can be used to address the contradictory water management issues and ensures highly efficient URFCs.

MATERIALS AND METHODS
Polymer-coated electrode fabrication
To fabricate the oxygen (O_2) electrode, iridium oxide (IrO_2) in a precursor solution was electrodeposited on Ti PTL (250 µm, Bekaert) at 0.65 V_{SCE} (~3 mA cm^{-2}) for 10 min. The Ir precursor solution, consisting of 0.01 M iridium(IV) chloride hydrate (99.95%, Ir 56.5%, Alfa-Aesar), oxalic acid [$(COOH)_2 \cdot 2H_2O$: 5 g liter^{-1}], and hydrogen peroxide (35% H_2O_2: 10 g liter^{-1}) in deionized (DI) water (18 megohms), was stirred for 3 days before the electrodeposition. As the OER catalyst for EC operation, electrodeposition of IrO_2 was reported with high mass activity at a low amount of catalysts (~0.15 mg cm^{-2}, thickness ~180 nm) coupled to Ti PTL (*29*). It forms IrO_2 catalysts with a specific surface area of ~13 m^2 g^{-1}_{Ir}. After preparing the IrO_2-electrodeposited PTLs, a shadow mask patterning process was performed using hydroxyl-terminated PDMS homopolymer (PDMS brush), poly(4-vinylpyridine) (P4VP) homopolymer, and metallic shadow masks with an LP (pitch, 250 µm; width, 125 µm) and an SP (pitch, 75 µm; width, 30 µm). The hydroxyl-terminated PDMS brush with a MW of 5 kg/mol was purchased from Polymer Source Inc., and P4VP homopolymer with a MW of 60 kg/mol was purchased from Sigma-Aldrich. For the patterning process, a heptane solution including the hydroxyl-terminated PDMS brush [2 weight % (wt %)] and the IPA solution including P4VP homopolymer (2 wt %) were prepared. To prevent the PDMS brush from coating the IrO_2-electrodeposited catalytic surface, a 150-µl P4VP homopolymer solution was sprayed on the IrO_2-electrodeposited side of PTLs (designated the bottom side of PTL). The temperature of PTLs during the spraying process was maintained at 80°C to rapidly evaporate the IPA. After passivating the IrO_2 catalyst surface with the P4VP homopolymer, a patterned P4VP layer was formed by spraying a 150-µl P4VP homopolymer solution through the shadow mask on the opposite side of Ti PTL (designated the top side of PTL). After that, the PDMS brush coating process was performed by drop casting the PDMS heptane solution on Ti PTL. After the surface of the micropatterned PTL was fully soaked by the PDMS brush solution, the heptane solvent was completely evaporated on a hot plate at 60°C. After that, the PDMS brush pattern was thermally cured for 3 hours in a vacuum oven at 200°C, so covalent links between the PDMS brush and the surface of PTLs

were established. Last, the PDMS brush–coated PTLs were washed with heptane, followed by IPA to remove the unattached PDMS brush and P4VP homopolymer. The fabrication process of the amphiphilic electrode is schematically illustrated in Fig. 1.

Physical characterization
The catalyst loading in e-IrO_2 was analyzed from inductively coupled plasma-optical emission spectroscopy (ICP-OES) (iCAP6500 Duo, Thermo Fisher Scientific). To analyze iridium in ICP-OES, e-IrO_2/Ti was pretreated before analysis as follows: (i) immerse the electrode in mixed solution including 5-ml HF and 15-ml aqua regia, (ii) heat the solution to 150°C, and (iii) add additional 15-ml aqua regia and 25-ml DI water to the solution. The surface chemical composition was analyzed by x-ray photoelectron spectroscopy (Thermo Fisher Scientific, K-alpha). The electrode morphology was examined by field-emission SEM (FE-SEM, Teneo Volume Scope) and by using OM (Cal Zeiss, Axioplan 2). NEXAFS analysis was performed at the soft x-ray 10D XAS KIST beamline of Pohang accelerator laboratory.

Half-cell electrochemistry
An AutoLab PGSTAT20 (Metrohm; AutoLab BV) potentiostat was used for the liquid half-cell tests. Pt wire and a saturated calomel electrode were used as the counter and reference electrodes, respectively. The IrO_2-coated active area was 9 cm^2, and the OER was performed at a fixed current density of 20 mA cm^{-2} using chronopotentiometry in 0.1 M $HClO_4$ electrolyte. A Nafion membrane was attached to the catalyst surface formed on PTLs through hot press so that the generated O_2 gas moved only through the opposite side of PTLs.

URFC device tests
To prepare the membrane electrode assembly (MEA) of the URFC device, Pt black (0.6 mg_{Pt} cm^{-2}) (high surface area, Alfa Aesar) and Pt/C (0.2 mg_{Pt} cm^{-2}) (46.6 wt %, Tanaka) were sprayed on the oxygen electrode side and the hydrogen electrode side of the membrane (CCM, Nafion 212), respectively. The catalyst slurry for the spray was prepared by mixing Pt black or Pt/C, Nafion ionomer solution (5 wt % Nafion), isopropyl alcohol, and DI water. Ionomer contents were 15 and 30 wt % for the Pt black and Pt/C catalyst layers, respectively. MEA (2.25 cm^2) composed of IrO_2-Ti PTL, Pt-coated N212, and carbon-PTL (Sigracet 39 BC) was hot pressed at 120°C and 43.6 MPa for 1 min (preheating: at 120°C without press for 2 min). For the single-cell assembly, MEA was placed between Ti and C bipolar plates with an assembly torque of 9.0 N·m. The performance of URFC was studied by current-voltage (*I-V*) analysis and electrochemical impedance spectroscopy (EIS) using a high-current potentiostat (HCP-803, Bio-Logic). The cell temperature was maintained at 80°C during URFC operation. During FC operation, the flow rate of both O_2 (or air) and H_2 gas was 200 ml min^{-1}. The relative humidity (RH) of the supplied gas was controlled to 100 and 65% for O_2 (or air) and H_2, respectively. In EC operation, DI water was provided to the oxygen electrode at a flow rate of 15 ml min^{-1}. *I-V* curves were obtained in the voltage scan from open circuit voltage (OCV) to 0.2 V_{Cell} for the FC and from 1.25 to 2.0 V_{Cell} for EC operation at a scan rate of 10 mV s^{-1}.

Scanning electrochemical microscopy
The ultramicroelectrode (UME, 25-µm Pt SECM probes, BioLogic) was purchased and polished before SECM measurements (M470, Bio-Logic SAS). An electrolyte solution composed of 5 mM potassium

ferricyanide (III) [$K_3Fe(CN)_6$, 99%, Sigma-Aldrich], 5 mM potassium hexacyanoferrate (II) trihydrate [$K_4Fe(CN)_6 \cdot 3H_2O$, ≥99.95%, Sigma-Aldrich], and 1 M potassium chloride (KCl, ≥99.9%, Sigma-Aldrich) in DI water was used to study the surface topology of Ti PTL in the SECM negative feedback mode. Sodium sulfate (0.5 M) (Na_2SO_4, ≥99.0%, Sigma-Aldrich) in DI water was used for the oxygen evolution reaction–oxygen reduction reaction (OER-ORR) experiments in the SECM SG/TC mode. For SECM measurements, the electrical connection to the Ti PTL substrates was made by copper wires and silver paste, and it was enclosed with an insulating epoxy. Only the refined electrode area was exposed to the electrolyte by attachment of a Kapton tape on the edge side of Ti PTL. The distance between the UME and Ti PTL surface, d, was estimated by three steps: (i) obtaining a negative approach curve of SECM to the Kapton film to confirm the distance of the tip from the substrate, (ii) moving the tip to above Ti PTL, and (iii) moving down as much as the Kapton film thickness, 73 μm (fig. S6).

SUPPLEMENTARY MATERIALS

Supplementary Materials for this article is available at http://advances.sciencemag.org/cgi/content/full/7/13/eabf7866/DC1

REFERENCES AND NOTES

1. T. M. Gür, Review of electrical energy storage technologies, materials and systems: Challenges and prospects for large-scale grid storage. *Energy Environ. Sci.* **11**, 2696–2767 (2018).
2. Y. Wang, D. Y. C. Leung, J. Xuan, H. Wang, A review on unitized regenerative fuel cell technologies, part-A: Unitized regenerative proton exchange membrane fuel cells. *Renew. Sustain. Energy Rev.* **65**, 961–977 (2016).
3. F. Mitlitsky, B. Myers, A. H. Weisberg, Regenerative fuel cell systems. *Energy Fuels* **12**, 56–71 (1998).
4. T. Sadhasivam, K. Dhanabalan, S.-H. Roh, T.-H. Kim, K.-W. Park, S. Jung, M. D. Kurkuri, H.-Y. Jung, A comprehensive review on unitized regenerative fuel cells: Crucial challenges and developments. *Int. J. Hydrog. Energy* **42**, 4415–4433 (2017).
5. U. Wittstadt, E. Wagner, T. Jungmann, Membrane electrode assemblies for unitised regenerative polymer electrolyte fuel cells. *J. Power Sources* **145**, 555–562 (2005).
6. G. Chen, H. Zhang, H. Zhong, H. Ma, Gas diffusion layer with titanium carbide for a unitized regenerative fuel cell. *Electrochim. Acta* **55**, 8801–8807 (2010).
7. S.-Y. Huang, P. Ganesan, H.-Y. Jung, B. N. Popov, Development of supported bifunctional oxygen electrocatalysts and corrosion-resistant gas diffusion layer for unitized regenerative fuel cell applications. *J. Power Sources* **198**, 23–29 (2012).
8. C. M. Hwang, M. Ishida, H. Ito, T. Maeda, A. Nakano, Y. Hasegawa, N. Yokoi, A. Kato, T. Yoshida, Influence of properties of gas diffusion layers on the performance of polymer electrolyte-based unitized reversible fuel cells. *Int. J. Hydrog. Energy* **36**, 1740–1753 (2011).
9. C. M. Hwang, M. Ishida, H. Ito, T. Maeda, A. Nakano, A. Kato, T. Yoshida, Effect of titanium powder loading in gas diffusion layer of a polymer electrolyte unitized reversible fuel cell. *J. Power Sources* **202**, 108–113 (2012).
10. T. Ioroi, T. Oku, K. Yasuda, N. Kumagai, Y. Miyazaki, Influence of PTFE coating on gas diffusion backing for unitized regenerative polymer electrolyte fuel cells. *J. Power Sources* **124**, 385–389 (2003).
11. H. Ito, T. Maeda, A. Nakano, C. M. Hwang, M. Ishida, N. Yokoi, Y. Hasegawa, A. Kato, T. Yoshida, Influence of different gas diffusion layers on the water management of polymer electrolyte unitized reversible fuel cell. *ECS Trans.* **33**, 945–954 (2010).
12. H.-Y. Jung, P. Ganesan, B. Popov, Development of high durability Bi-functional oxygen electrode for unitized regenerative fuel cell (URFC). *ECS Trans.* **25**, 1261–1269 (2009).
13. L. Castanheira, L. Dubau, M. Mermoux, G. Berthome, N. Caqué, E. Rossinot, M. Chatenet, F. Maillard, Carbon corrosion in proton-exchange membrane fuel cells: From model experiments to real-life operation in membrane electrode assemblies. *ACS Catal.* **4**, 2258–2267 (2014).
14. L. Castanheira, W. O. Silva, F. H. B. Lima, A. Crisci, L. Dubau, F. Maillard, Carbon corrosion in proton-exchange membrane fuel cells: Effect of the carbon structure, the degradation protocol, and the gas atmosphere. *ACS Catal.* **5**, 2184–2194 (2015).
15. Q. Feng, X.-Z. Yuan, G. Liu, B. Wei, Z. Zhang, H. Li, H. Wang, A review of proton exchange membrane water electrolysis on degradation mechanisms and mitigation strategies. *J. Power Sources* **366**, 33–55 (2017).
16. S.-E. Jang, H. Kim, Effect of water electrolysis catalysts on carbon corrosion in polymer electrolyte membrane fuel cells. *J. Am. Chem. Soc.* **132**, 14700–14701 (2010).
17. P. Lettenmeier, S. Kolb, N. Sata, A. Fallisch, L. Zielke, S. Thiele, A. S. Gago, K. A. Friedrich, Comprehensive investigation of novel pore-graded gas diffusion layers for high-performance and cost-effective proton exchange membrane electrolyzers. *Energy Environ. Sci.* **10**, 2521–2533 (2017).
18. T. Schuler, J. M. Ciccone, B. Krentscher, F. Marone, C. Peter, T. J. Schmidt, F. N. Büchi, Hierarchically structured porous transport layers for polymer electrolyte water electrolysis. *Adv. Energy Mater.* **10**, 1903216 (2020).
19. H. Ito, T. Maeda, A. Nakano, C. M. Hwang, M. Ishida, A. Kato, T. Yoshida, Effect of titanium powder loading in microporous layer on a polymer electrolyte unitized reversible fuel cell. *ECS Trans.* **41**, 469–477 (2011).
20. I. Bita, J. K. W. Yang, Y. S. Jung, C. A. Ross, E. L. Thomas, K. K. Berggren, Graphoepitaxy of self-assembled block copolymers on two-dimensional periodic patterned templates. *Science* **321**, 939–943 (2008).
21. S. Cha, C. Kim, Poly(dimethylsiloxane) stamp coated with a low-surface-energy, diffusion-blocking, covalently bonded perfluoropolyether layer and its application to the fabrication of organic electronic devices by layer transfer. *ACS Appl. Mater. Interfaces* **10**, 24003–24012 (2018).
22. Y. S. Jung, C. A. Ross, Orientation-controlled self-assembled nanolithography using a polystyrene-polydimethylsiloxane block copolymer. *Nano Lett.* **7**, 2046–2050 (2007).
23. J. M. Kim, Y. H. Hur, J. W. Jeong, T. W. Nam, J. H. Lee, K. Jeon, Y. Kim, Y. S. Jung, Block copolymer with an extremely high block-to-block interaction for a significant reduction of line-edge fluctuations in self-assembled patterns. *Chem. Mater.* **28**, 5680–5688 (2016).
24. W.-L. Chen, R. Cordero, H. Tran, C. K. Ober, 50th anniversary perspective: Polymer brushes: Novel surfaces for future materials. *Macromolecules* **50**, 4089–4113 (2017).
25. O. Azzaroni, Polymer brushes here, there, and everywhere: Recent advances in their practical applications and emerging opportunities in multiple research fields. *J. Polym. Sci. Polym. Chem.* **50**, 3225–3258 (2012).
26. N. Ayres, Polymer brushes: Applications in biomaterials and nanotechnology. *Polym. Chem.* **1**, 769–777 (2010).
27. H. Ungan, A. B. Yurtcan, PEMFC catalyst layer modification with the addition of different amounts of PDMS polymer in order to improve water management. *Int. J. Energy Res.* **43**, 5946–5958 (2019).
28. S. Choe, B.-S. Lee, M. K. Cho, H.-J. Kim, D. Henkensmeier, S. J. Yoo, J. Y. Kim, S. Y. Lee, H. S. Park, J. H. Jang, Electrodeposited IrO_2/Ti electrodes as durable and cost-effective anodes in high-temperature polymer-membrane-electrolyte water electrolyzers. *Appl. Catal. B Environ.* **226**, 289–294 (2018).
29. A. Lim, J. Kim, H. J. Lee, H.-J. Kim, S. J. Yoo, J. H. Jang, H. Young Park, Y.-E. Sung, H. S. Park, Low-loading IrO_2 supported on Pt for catalysis of PEM water electrolysis and regenerative fuel cells. *Appl. Catal. B Environ.* **272**, 118955 (2020).
30. S.-Y. Park, W.-H. Sul, Y.-J. Chang, A study on the selectivity of toluene/ethanol mixtures on the micellar and ordered structures of poly(styrene-*b*-4-vinylpyridine) using small-angle X-ray scattering, generalized indirect fourier transform, and transmission electron microscopy. *Macromolecules* **40**, 3757–3764 (2007).
31. K. Efimenko, W. E. Wallace, J. Genzer, Surface modification of Sylgard-184 poly(dimethyl siloxane) networks by ultraviolet and ultraviolet/ozone treatment. *J. Coll. Interface Sci.* **254**, 306–315 (2002).
32. A. D. Winter, E. Larios, F. M. Alamgir, C. Jaye, D. Fischer, E. M. Campo, Near-edge x-ray absorption fine structure studies of electrospun poly(dimethylsiloxane)/poly(methyl methacrylate)/multiwall carbon nanotube composites. *Langmuir* **29**, 15822–15830 (2013).
33. J. M. Kim, J.-H. Kim, J. Kim, Y. Lim, Y. Kim, A. Alam, J. Lee, H. Ju, H. C. Ham, J. Y. Kim, Synergetic structural transformation of Pt electrocatalyst into advanced 3D architectures for hydrogen fuel cells. *Adv. Mater.* **32**, 2002210 (2020).
34. M. Geng, Z. Duan, Prediction of oxygen solubility in pure water and brines up to high temperatures and pressures. *Geochim. Cosmochim. Acta* **74**, 5631–5640 (2010).
35. B. O. Emmanuel, P. Barendse, J. Chamier, Effect of anode and cathode reletive humidity variance and pressure gradient on single cell PEMFC performance, in *IEEE Energy Conversion Congress and Exposition (ECCE)* (2018), pp. 3608–3615.
36. J. Lopata, Z. Kang, J. Young, G. Bender, J. W. Weidner, S. Shimpalee, Effects of the transport/catalyst layer interface and catalyst loading on mass and charge transport phenomena in polymer electrolyte membrane water electrolysis devices. *J. Electrochem. Soc.* **167**, 064507 (2020).
37. J. C. Garcia-Navarro, M. Schulze, K. A. Friedrich, Measuring and modeling mass transport losses in proton exchange membrane water electrolyzers using electrochemical impedance spectroscopy. *J. Power Sources* **431**, 189–204 (2019).
38. S. A. Grigoriev, P. Millet, V. I. Porembsky, V. N. Fateev, Development and preliminary testing of a unitized regenerative fuel cell based on PEM technology. *Int. J. Hydrog. Energy* **36**, 4164–4168 (2011).
39. S. Choe, B.-S. Lee, J. H. Jang, Effects of Diffusion Layer (DL) and ORR Catalyst (MORR) on the performance of MORR/IrO_2/DL electrodes for PEM-type unitized regenerative fuel cells. *J. Electrochem. Sci. Technol.* **8**, 7–14 (2017).

40. P. Millet, R. Ngameni, S. A. Grigoriev, V. N. Fateev, Scientific and engineering issues related to PEM technology: Water electrolysers, fuel cells and unitized regenerative systems. *Int. J. Hydrog. Energy* **36**, 4156–4163 (2011).

41. J. C. Cruz, V. Baglio, S. Siracusano, R. Ornelas, L. G. Arriaga, V. Antonucci, A. S. Aricò, Nanosized Pt/IrO$_2$ electrocatalyst prepared by modified polyol method for application as dual function oxygen electrode in unitized regenerative fuel cells. *Int. J. Hydrog. Energy* **37**, 5508–5517 (2012).

42. J. X. Liu, H. Guo, X. M. Yuan, F. Ye, C. F. Ma, Experimental investigation on two-phase flow in a unitized regenerative fuel cell during mode switching from water electrolyzer to fuel cell. *Int. J. Energy Res.* **42**, 2823–2834 (2018).

43. B. Krishnamurthy, S. Deepalochani, Performance of platinum black and supported platinum catalysts in a direct methanol fuel cell. *Int. J. Electrochem. Sci.* **4**, 386–395 (2009).

44. T. R. Ralph, G. A. Hards, J. E. Keating, S. A. Campbell, D. P. Wilkinson, M. Davis, J. St-Pierre, M. C. Johnson, Low cost electrodes for proton exchange membrane fuel cells: Performance in single cells and Ballard stacks. *J. Electrochem. Soc.* **144**, 3845–3857 (1997).

45. G. C. da Silva, M. R. Fernandes, E. A. Ticianelli, Activity and stability of Pt/IrO$_2$ bifunctional materials as catalysts for the oxygen evolution/reduction reactions. *ACS Catal.* **8**, 2081–2092 (2018).

46. G. C. da Silva, K. J. J. Mayrhofer, E. A. Ticianelli, S. Cherevko, Dissolution stability: The major challenge in the regenerative fuel cells bifunctional catalysis. *J. Electrochem. Soc.* **165**, F1376–F1384 (2018).

47. S. Zhang, X.-Z. Yuan, J. N. C. Hin, H. Wang, K. A. Friedrich, M. Schulze, A review of platinum-based catalyst layer degradation in proton exchange membrane fuel cells. *J. Power Sources* **194**, 588–600 (2009).

48. P. Zhang, S.-Y. Huang, B. N. Popov, Mesoporous tin oxide as an oxidation-resistant catalyst support for proton exchange membrane fuel cells. *J. Electrochem. Soc.* **157**, B1163–B1172 (2010).

49. D. Kunwar, S. Zhou, A. DeLaRiva, E. J. Peterson, H. Xiong, X. I. Pereira-Hernández, S. C. Purdy, R. ter Veen, H. H. Brongersma, J. T. Miller, H. Hashiguchi, L. Kovarik, S. Lin, H. Guo, Y. Wang, A. K. Datye, Stabilizing high metal loadings of thermally stable platinum single atoms on an industrial catalyst support. *ACS Catal.* **9**, 3978–3990 (2019).

50. J. Miyake, M. Kusakabe, A. Tsutsumida, K. Miyatake, Remarkable reinforcement effect in sulfonated aromatic polymers as fuel cell membrane. *ACS Appl. Energ. Mater.* **1**, 1233–1238 (2018).

51. S. Giancola, M. Zatoń, Á. Reyes-Carmona, M. Dupont, A. Donnadio, S. Cavaliere, J. Rozière, D. J. Jones, Composite short side chain PFSA membranes for PEM water electrolysis. *J. Membr. Sci.* **570–571**, 69–76 (2019).

Citation: A. Lim, H.-Y. Jeong, Y. Lim, J. Y. Kim, H. Y. Park, J. H. Jang, Y.-E. Sung, J. M. Kim, H. S. Park, Amphiphilic Ti porous transport layer for highly effective PEM unitized regenerative fuel cells. *Sci. Adv.* **7**, eabf7866 (2021).